



CHORUS

This is the accepted manuscript made available via CHORUS. The article has been published as:

Electronic chirality in the metallic ferromagnet $\text{Fe}_{1/3}\text{TaS}_2$

S. Fan, I. Manuel, Amal al-Wahish, K. R. O'Neal, K. A. Smith, C. J. Won, J. W. Kim, S.-W. Cheong, J. T. Haraldsen, and J. L. Musfeldt

Phys. Rev. B **96**, 205119 — Published 13 November 2017

DOI: [10.1103/PhysRevB.96.205119](https://doi.org/10.1103/PhysRevB.96.205119)

Electronic chirality in the metallic ferromagnet $\text{Fe}_{1/3}\text{TaS}_2$

S. Fan,¹ I. Manuel,² Amal al-Wahish,³ K. R. O'Neal,³ K. A. Smith,³ C. J. Won,⁴ J. W. Kim,⁵ S. -W. Cheong,^{4,5} J. T. Haraldsen,² and J. L. Musfeldt^{1,3}

¹*Department of Physics and Astronomy, University of Tennessee, Knoxville, Tennessee, 37996, USA*

²*Department of Physics, University of North Florida, Jacksonville, Florida 32224, USA*

³*Department of Chemistry, University of Tennessee, Knoxville, Tennessee, 37996, USA*

⁴*Laboratory for Pohang Emergent Materials and Max Plank POSTECH Center for Complex Phase Materials, Pohang University of Science and Technology, Pohang 790-784, Korea*

⁵*Rutgers Center for Emergent Materials and Department of Physics and Astronomy, Rutgers University, Piscataway, New Jersey 08854, USA*

We bring together optical spectroscopy and first principles calculations to reveal the electronic properties of the chiral ferromagnet $\text{Fe}_{1/3}\text{TaS}_2$. Signatures of chirality are superimposed upon a complex free carrier response that emanates from both Ta and Fe bands. These include a honeycomb charge density pattern in the Fe layer and a hole \rightarrow electron pocket crossover at the K-point, low energy excitations between spin split bands that cross the Fermi surface, and clustered rather than well-separated on-site and charge transfer excitations. These findings advance the understanding of intercalation and symmetry breaking on the fundamental excitations in metallic chalcogenides.

I. INTRODUCTION

Research on engineered superlattice materials has blossomed in recent years due to the discovery of unexpected properties deriving from interface effects¹⁻⁴. Naturally occurring superlattices like intercalated oxides and chalcogenides are of contemporary interest as well. Examples include the chiral helimagnets $\text{Cr}_{1/3}\text{NbS}_2$ and $[\text{Pb}_2\text{BiS}_3][\text{AuTe}_2]$, superconducting Pd-intercalated IrTe_2 , and interlayer I-doped BiOIO_3 nanoplates⁵⁻⁹. The chiral ferromagnet $\text{Fe}_{1/3}\text{TaS}_2$ attracted our attention in this context¹⁰. This system is based upon 2H- TaS_2 ^{11,12} and has a set of stable, well-ordered intercalation plateaus at $x=1/4$ and $1/3$ [Fig. 1(a-c)]¹⁰. The pattern of Fe centers is responsible for the non-centrosymmetric, chiral space group of the $x=1/3$ system¹⁰. Intercalation suppresses the charge density wave transitions¹³, and magnetic transitions arise at 160 and 35 K for the $x=1/4$ and $1/3$ materials, respectively^{10,14,15}. Large magnetoresistances and high coercivities have been reported as well¹⁶. Moreover, the atomically thin Fe layers in Fe_xTaS_2 display fascinating domain wall symmetries and domain patterns¹⁰. That in the $x=1/3$ system is $Z_2 \times Z_3$ ¹⁷. In this work, we show that signatures of chirality in $\text{Fe}_{1/3}\text{TaS}_2$ are deeply and subtly embedded within the electronic structure, reminiscent of the hidden Fermi surface nesting that causes charge density wave ordering in low-dimensional materials¹⁸.

In order to explore intercalation effects on the fundamental excitations of a chiral ferromagnet, we measured the spectroscopic response of $\text{Fe}_{1/3}\text{TaS}_2$ and compared our findings with the $x=0$ and $1/4$ compounds and complementary first principles calculations. The main finding is that there is a strong influence of the Fe layer on the properties of the compound, perhaps stronger than what would be expected for van der Waals interlayer bonding. Strikingly, separation of chalcogenide slabs by atomically thin layers of iron introduces a second free carrier re-

sponse due to a peak in the density of states at the Fermi level along with a set of localized bands that are connected to the density and pattern of the Fe centers. Symmetry breaking in $\text{Fe}_{1/3}\text{TaS}_2$ is evident in charge density patterns that progress from triangular to Kagomé to honeycomb, the hole \rightarrow electron pocket crossover near the K-point, and the characteristic set of low energy electronic excitations between spin split bands that cross the Fermi surface. Signatures of chirality are firmly embedded in the bound carrier excitations as well, which we analyze by tracking trends in the hybridized Fe- and Ta-containing bands. Importantly, these effects are exposed in a metallic system, so in addition to providing opportunities to compare correlation vs. spin-orbit effects in Fe-containing chalcogenides¹⁹⁻²¹, they reveal ideas that may be useful in the hunt for metallic ferroelectrics^{22,23}.

II. METHODS

Single crystals of Fe_xTaS_2 ($x=1/4$ and $1/3$) were grown by chemical vapor transport techniques as described previously, and the Fe concentration was confirmed by magnetization¹⁰. We measured *ab*-plane reflectance using a series of spectrometers (4 meV-6.5 eV; 4.2-300 K) and employed a Kramers-Kronig analysis to extract the optical constants. Traditional peak fitting techniques were also employed as appropriate. Computational work was performed using Density Functional Theory provided by Atomistix Toolkit^{24,25}. Using a spin-polarized generalized gradient approach with an on-site potential (SGGA+*U*), the electronic structure, density of states (DOS), and electron density were determined²⁶. The on-site potential localizes the Fe electrons that contribute to the overall magnetic moment; we find $3.8 \mu_B$.

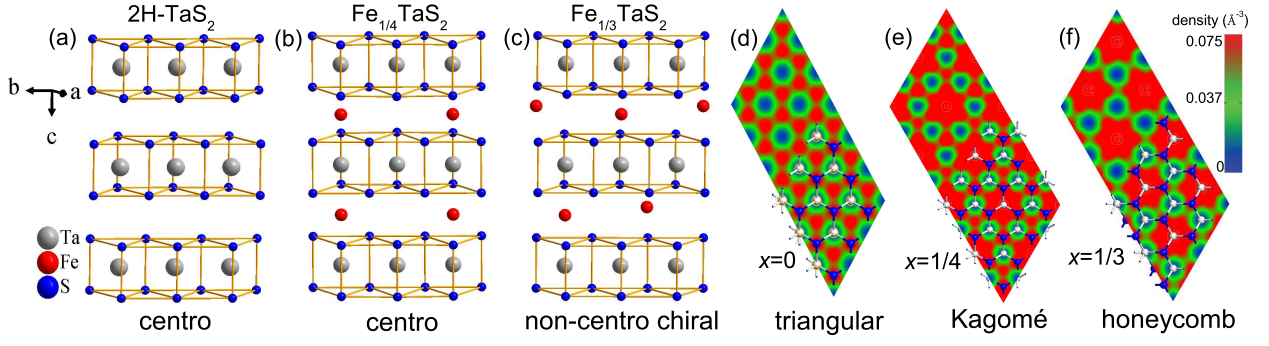
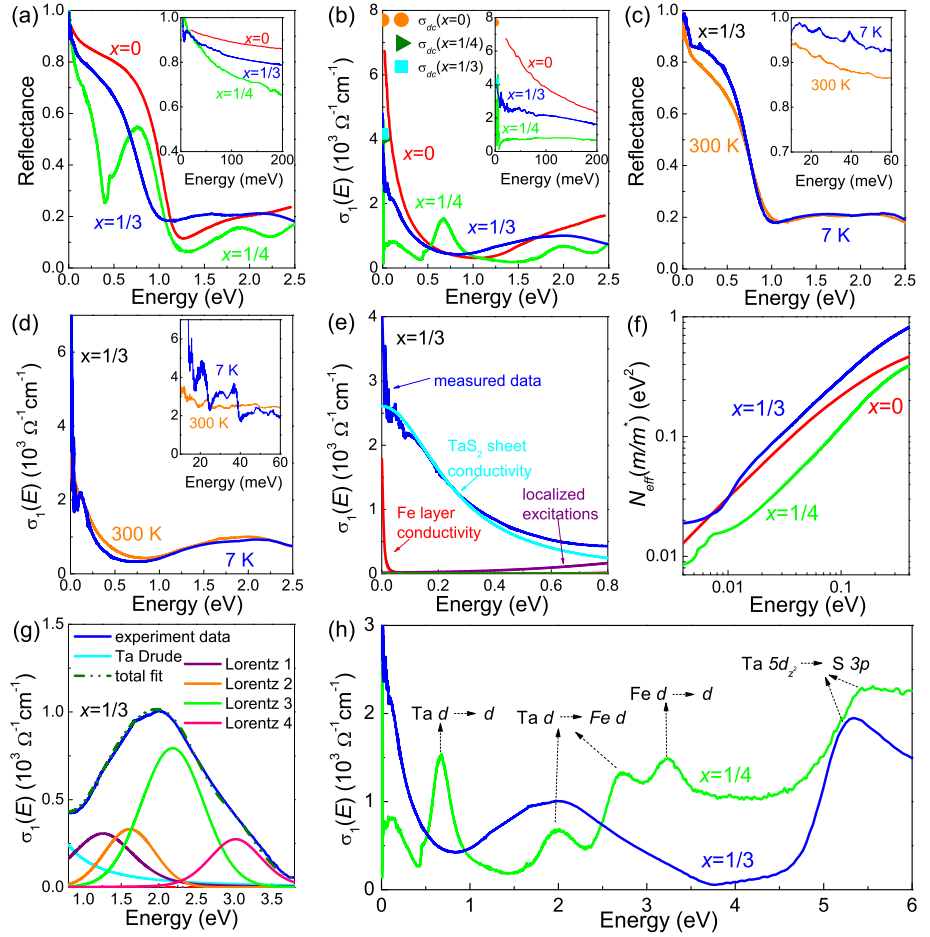


FIG. 1. (a) Crystal structure of 2H-TaS₂ in the centrosymmetric $P6_3/mmc$ space group²⁷. Ta⁴⁺ is at the center of a prism formed by six S²⁻ centers. (b) Fe_{1/4}TaS₂ also belongs to the $P6_3/mmc$ space group¹⁰. Each Fe center is octahedrally coordinated by six S²⁻ atoms. Stacking along c is AA type, yielding an expanded $2a \times 2a$ superlattice. (c) The structure of Fe_{1/3}TaS₂ is non-centrosymmetric and chiral (space group $P6_322$)¹⁰. Stacking along c is alternating (AB) type, yielding a $\sqrt{3}a \times \sqrt{3}a$ superlattice. (d, e, f) Projected charge density in the Fe plane for 2H-TaS₂, Fe_{1/4}TaS₂, and Fe_{1/3}TaS₂.

FIG. 2. (a) Reflectance of Fe_{1/4}TaS₂, Fe_{1/3}TaS₂, and 2H-TaS₂. The 2H-TaS₂ data is reproduced from Ref. 11. Inset: close-up view of the low energy response. (b) Optical conductivity of these materials. Literature values of the dc conductivity^{28–30} are also plotted; $\sigma_1(E)$ extrapolates to these values reasonably well. (c) Reflectance of Fe_{1/3}TaS₂ at 300 and 7 K. (d) Optical conductivity of the $x=1/3$ material at 300 and 7 K. Inset displays a close-up view of low energy response. (e) Close-up view of the two Drude oscillators needed to fit the response of Fe_{1/3}TaS₂. (f) Oscillator strength sum rule for the $x=0$, 1/4, and 1/3 compounds. (g) Drude-Lorentz fit of the localized excitations in Fe_{1/3}TaS₂. (h) Optical conductivity of Fe_{1/4}TaS₂ and Fe_{1/3}TaS₂ highlighting the difference in the localized excitations.



III. RESULT AND DISCUSSION

Figure 2(a,b) displays the reflectance and optical conductivity of Fe_{1/4}TaS₂ and Fe_{1/3}TaS₂ compared with that of 2H-TaS₂¹¹. Intercalation dramatically changes the character of the optical conductivity. The trend is non-monotonic, with the Drude response in the $x=1/3$

system being more robust than for $x=1/4$. Although this family of transition metal dichalcogenides is metallic, there are several small structures between 10 and 40 meV in the $x=1/3$ compound that are not completely screened. They are present at 300 K but much more evident at low temperature [Fig. 2(c,d)]. The energy scale of these features is consistent with assignment as ei-

ther phonons or electronic excitations between spin split bands. Temperature effects are overall modest.

Figure 2(e) displays a close-up view of the Drude-Lorentz fit to the optical conductivity of $\text{Fe}_{1/3}\text{TaS}_2$. Two Drude functions are needed to capture the response. The two-component nature of the free carrier behavior is due to the superposition of Fe and TaS_2 layer conductivities. The former has only about 1% of the oscillator strength of the latter. Compared to 2H- TaS_2 , intercalation at the $x=1/3$ level reduces the oscillator strength associated with the TaS_2 slab by approximately 40%, the plasma frequency by 15%, and the relaxation time by 35% [Table I]. These trends quantify the fact that the TaS_2 layers are well isolated between Fe sheets. The Drude associated with the Fe layer is much narrower than that deriving from the Ta bands (which so prominently cross the Fermi surface).

TABLE I. Drude parameters of Fe_xTaS_2 ($x=0, 1/4, 1/3$) obtained from fits to the optical conductivity at 300 K. Error bars on the fit parameters are on the order of 1%, with the exception of the very narrow Fe Drude in the $x=1/4$ material, where the error bars are on the order of 5%.

| Materials | Oscillator strength (eV^2) | Plasma freq (eV) | Relaxation time (s) |
|-------------------------------|---------------------------------------|------------------|-----------------------|
| 2H- TaS_2 | 0.18 | 1.19 | 2.5×10^{-14} |
| $\text{Fe}_{1/4}\text{TaS}_2$ | | | |
| Fe Drude | 0.37×10^{-3} | 0.02 | 3.5×10^{-12} |
| TaS_2 Drude | 0.038 | 0.66 | 1.3×10^{-14} |
| $\text{Fe}_{1/3}\text{TaS}_2$ | | | |
| Fe Drude | 1.78×10^{-3} | 0.24 | 7.5×10^{-13} |
| TaS_2 Drude | 0.11 | 1.02 | 1.6×10^{-14} |

A similar situation arises in $\text{Fe}_{1/4}\text{TaS}_2$ where fits to the optical response require two Drude oscillators. The metallic character is weaker than in the $x=1/3$ system due to a different degree of mixing of the hybridized Ta + Fe d bands crossing the Fermi level. The Fe Drude is extremely narrow because the distance between Fe centers is quite large (6.614 Å for $x=1/4$ vs. 5.737 Å for $x=1/3$), an effect that is evident in the charge density patterns. The lower density of atomic centers in the Fe sheet of the $x=1/4$ material reduces overlap and increases the relaxation time [Table I]. An oscillator strength analysis [Fig. 2(f)] provides additional evidence for a narrow Drude³¹.

Turning our attention to the higher energy portion of the spectra, the pattern of well-separated on-site and charge transfer excitations in the $x=1/4$ material and the superimposed set of features in the $x=1/3$ system seem dramatically different [Fig. 2(h)]. Closer examination, however, reveals that the localized and charge transfer excitations reflect the trend in the Fe levels. In the $x=1/4$ system, we assign the band centered at 0.7 eV as a minority channel Ta $d \rightarrow \text{Ta } d$ excitation and those at 2.0, and 2.6 eV as Ta $d \rightarrow \text{Fe } d$ charge transfer excitations in the spin-down channel. The 3.2 eV peak is assigned to a minority channel Fe $d \rightarrow \text{Fe } d$ excitations. Four excita-

tions also appear in the spectrum of the $x=1/3$ material, but they are clustered together at 1.2, 1.6, 2.2, and 3 eV [Fig. 2(g)], and the assignment changes somewhat. These excitations are superimposed at overall higher energy because the Fe bands have moved up in energy and are significantly more disperse compared to those in the $x=1/4$ system. This allows the Fe levels to hybridize with the Ta bands around 2 eV. There is also a band centered near 5.3 eV in both materials. In 2H- TaS_2 , it is assigned as a Ta $5d_{z^2}$ conduction band to S $3p$ valence band excitation³². The characterization shifts to greater d -band contributions in the $x=1/4$ and $1/3$ systems.

Figure 3 displays the calculated electronic band structure and projected density of states for the three systems of interest. We used this band structure to assign all of the optical excitations in these materials. Where comparable, our findings are in good agreement with prior work^{13,33,34}. In our analysis of 2H- TaS_2 , there exist two distinct Ta-derived bands crossing the Fermi level [Fig. 3(a)] that are characteristic of Dirac lines³⁵. These bands make the system metallic and produce excitations to the bands near 3.5 eV. These aspects of the electronic structure remain recognizable even with the addition of Fe and hybridization with Fe-related bands. Electron and hole pockets are predicted at the M- and K-points, re-

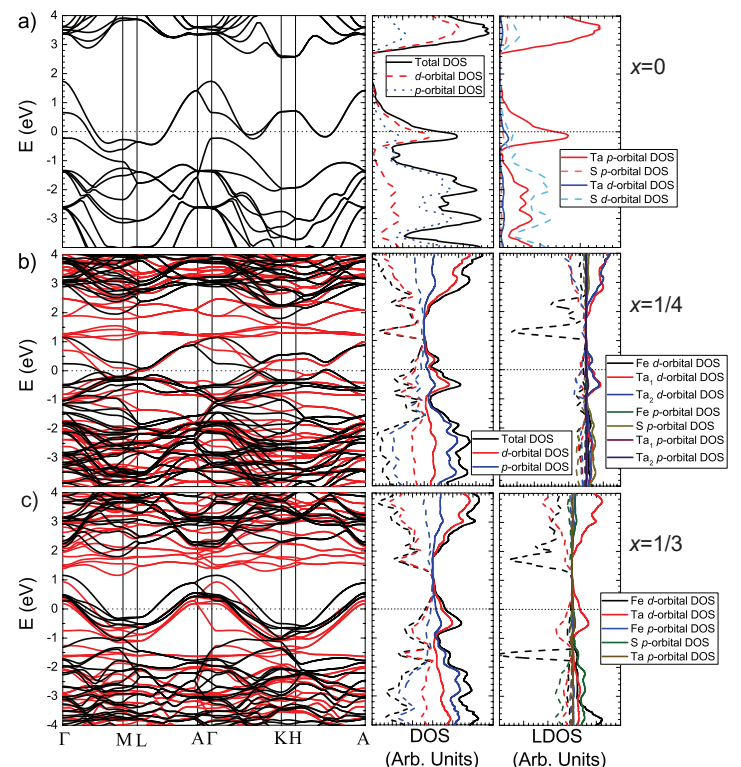


FIG. 3. Calculated electronic band structure and DOS (total, partial, and local) for (a) 2H- TaS_2 , (b) $\text{Fe}_{1/4}\text{TaS}_2$, and (c) $\text{Fe}_{1/3}\text{TaS}_2$. The black and red bands in the electronic structure and the solid and dashed lines in the DOS plots denote the spin-up and spin-down channels, respectively.

spectively.

Introduction of an atomically thin layer of Fe into the van der Waals gap modifies the electronic structure profoundly. Our calculations employ a Hubbard U (similar to Ref. 13) which acts to localize the Fe bands, leaving only a remnant of Fe density at the Fermi level. Localization is thus responsible for the weak metallicity of the Fe layer in the $x=1/4$ system (evidenced by small but distinct second Drude oscillator in the inset of Fig. 2(b)). When Fe density increases ($x=1/3$), orbital overlap is improved, and the localized Fe bands are swept upward. This gives greater metallicity to the Fe layer because density at the Fermi surface is larger and, at the same time, raises the energy of the localized Fe bands which allows them to hybridize with the Ta-derived bands. This process strengthens the Fe-derived Drude and makes the localized excitations seem to disappear. The persistence of the Dirac lines produced by the TaS₂ slabs at high symmetry points demonstrates that these modifications are due to differences in overall electronic behavior rather than intercalation-induced structural changes.

To further examine the connection between symmetry and electronic structure, we projected the charge density onto the plane defined by the Fe centers [Fig. 1(d-f)]. With these renderings, we see that as the Fe concentration increases, the overlap between Fe sites becomes stronger and more direct, and at the 1/3 level, the Fe centers even move out of the way of the S ions allowing for more direct orbital overlap. Thus, while the dominant Drude response is connected with free carriers in the Ta bands, the Fe ions introduce a second metallic signature - consistent with our spectroscopic findings. Remarkably, these contour plots also reveal a progression from a triangular ($x=0$) to Kagomé ($x=1/4$) to honeycomb ($x=1/3$) charge density pattern [Fig. 1(d-f)]. The latter is (ironically) indicative of increased symmetry in the Fe plane - even though the overall crystal symmetry is reduced.

Another consequence of the evolving charge density pattern can be seen by comparing the electronic structure at the M and K symmetry points. In the centrosymmetric case [Fig. 3(a, b)], the M-point sports an electron pocket whereas the K-point has a hole pocket. However, in the non-centrosymmetric case [Fig. 3(c)], both locations host electron pockets. This hole to electron pocket crossover at the K-point, while certainly not simple, may be observable in a Hall measurement and could have important implications for the field of valleytronics³⁶. We note that the crossover to electron pockets in Fe_{1/3}TaS₂ is not just due to increased carrier density from the Fe centers (although additional density does accumulate at the K-point) but rather due to the manner in which Fe breaks crystal symmetry. Therefore, a gating experiment that merely raises and lowers the Fermi energy against a rigid band structure would not show this effect.

Finally, we point out that broken inversion symmetry in the $x=1/3$ material is predicted to lift the spin degeneracy of the electronic bands near the Fermi surface [Fig. 4(a)]. The energy scale of this splitting is on the order of

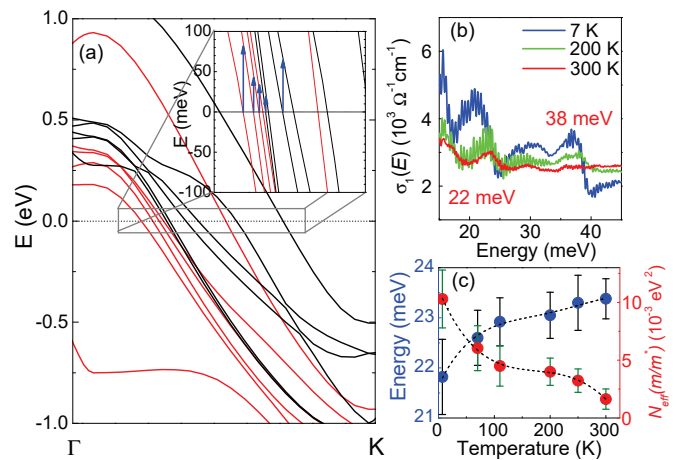


FIG. 4. (a) Close up view of the band structure of Fe_{1/3}TaS₂ between the Γ and K-points. Inset: low energy excitations on the order of a few tens of meV due to the band splitting. (b) Temperature dependence of the optical conductivity of the $x=1/3$ materials in the vicinity of the 22 and 38 meV excitations. (c) Peak position and oscillator strength of the 22 meV feature as a function of temperature.

tens of meV, consistent with the aforementioned features at 22 and 38 meV in the optical conductivity. Figure 4(b) displays a close-up view of these structures. Although the excitation energies are in line with what might be expected for electronic band splitting, assignment is not straightforward because they are also consistent with phonon positions³⁷. As shown in Fig. 4 (b, c), decreasing temperature red shifts the 22 and 38 meV structures and increases the oscillator strength.³⁸ Both trends differ from what is expected for phonons on a conducting background³⁹. Moreover, we do not anticipate significant differences in phonon effects between the $x=1/4$ and 1/3 materials, which again argues against a phonon interpretation. Returning to our picture of low energy spin split electronic excitations, there are several bands crossing the Fermi energy with vertical band-to-band transitions in the correct energy range [Fig. 4(a)]. Recent models of Rashba splitting in BiTeI⁴⁰ suggest that thermal expansion and electron-phonon coupling effects combine to reduce the effective Rashba parameter and smear the gap(s) at elevated temperatures. Of course, while the 2H- structures technically lack inversion symmetry, they do have a vertical mirror plane, so we do not anticipate the same kind of strong inversion-breaking Rashba effects that are observed in BiTeI⁴¹. Additional evidence that the 22 and 38 meV excitations may be electronic in origin comes from the $x=1/4$ system where these features are not observed.

IV. CONCLUSION

To summarize, we combined optical spectroscopy and first principles calculations to reveal intercalation and

symmetry breaking effects in the non-centrosymmetric, chiral ferromagnet $\text{Fe}_{1/3}\text{TaS}_2$. The main finding is that there is a strong influence of the Fe layer on the properties of the compound, perhaps stronger than what would be expected for van der Waals interlayer bonding. Signatures of chirality include a honeycomb charge density pattern and hole \rightarrow electron pocket crossover, low energy excitations between spin split bands, and overlapping on-site and charge transfer excitations. These findings are useful for the development of low symmetry multifunctional chalcogenides.

ACKNOWLEDGMENTS

Research at Tennessee is supported by the U.S. Department of Energy, Office of Basic Energy Sciences, Materials Science Division under award DE-FG02-01ER45885. JTH acknowledges funding from the Institute for Materials Science at Los Alamos National Laboratory. Work at Rutgers is supported by the NSF-DMREF program (DMR-1629059). Research at Postech is funded by the Max Planck POSTECH/KOREA Research Initiative Program 2011-0031558 through NRF of Korea funded by MEST. We thank A. V. Balatsky and D. H. Vanderbilt for useful discussions.

-
- ¹ H. Y. Hwang, Y. Iwasa, M. Kawasaki, B. Keimer, N. Nagaosa, and Y. Tokura, *Nat. Mater.* **11**, 103 (2012).
- ² S. Singh, J. T. Haraldsen, J. Xiong, E. M. Choi, P. Lu, D. Yi, X. -D. Wen, J. Liu, H. Wang, Z. Bi, P. Yu, M. R. Fitzsimmons, J. L. MacManus-Driscoll, R. Ramesh, A. V. Balatsky, J. -X. Zhu, and Q. X. Jia, *Phys. Rev. Lett.* **113**, 047204 (2014).
- ³ J. A. Mundy, C. M. Brooks, M. E. Holtz, J. A. Moyer, H. Das, A. F. Rebola, J. T. Heron, J. D. Clarksen, S. M. Disseler, Z. Liu, A. Farhan, R. Held, R. Hovden, E. Padgett, Q. Mao, H. Paik, R. Misra, L. F. Kourkoutis, E. Arenholz, A. Scholl, J. A. Borchers, W. D. Ratcliff, R. Ramesh, C. J. Fennie, P. Schiffer, D. A. Muller and D. G. Schlom, *Nature* **537**, 523 (2016).
- ⁴ B. -W. Li, M. Osada, Y. Ebina, S. Ueda, and T. Sasaki, *J. Am. Chem. Soc.* **138**, 7621 (2016).
- ⁵ Y. Sun, T. Xiong, F. Dong, H. Huang, and W. Cen, *Chem. Commun.* **52**, 8243 (2016).
- ⁶ Y. Togawa, T. Koyama, K. Takayanagi, S. Mori, Y. Kousaka, J. Akimitsu, S. Nishihara, K. Inoue, A. S. Ovchinnikov, and J. Kishine, *Phys. Rev. Lett.* **108**, 107202 (2012).
- ⁷ N. J. Ghimire, M. A. McGuire, D. S. Parker, B. Sipos, S. Tang, J. -Q. Yan, B. C. Sales, and D. Mandrus, *Phys. Rev. B* **87**, 104403 (2013).
- ⁸ J. J. Yang, Y. J. Choi, Y. S. Oh, A. Hogan, Y. Horibe, K. Kim, B. I. Min, and S. -W. Cheong, *Phys. Rev. Lett.* **108**, 116402 (2012).
- ⁹ L. Fang, J. Im, W. DeGottardi, Y. Jia, A. Glatz, K. A. Matveev, W.-K. Kwok, G. W. Crabtree, and M. G. Kanatzidis, *Sci. Reports* **6**, 35313 (2016).
- ¹⁰ Y. Horibe, J. Yang, Y. H. Cho, X. Luo, S. B. Kim, Y. S. Oh, F. T. Huang, T. Asada, M. Tanimura, D. Jeong, and S. W. Cheong, *J. Am. Chem. Soc.* **136**, 8368 (2014).
- ¹¹ W. Z. Hu, G. Li, J. Yan, H. H. Wen, G. Wu, X. H. Chen, and N. L. Wang, *Phys. Rev. B* **76**, 045103 (2007).
- ¹² S. S. P. Parkin and R. H. Friend, *Phil. Mag. B*, **41**, 65 (1980).
- ¹³ S. Mankovsky, K. Chadova, D. Kodderitzsch, J. Minar, H. Ebert, and W. Bensch, *Phys. Rev. B* **92**, 144413 (2015).
- ¹⁴ Th. Danz, Q. Liu, X. D. Zhu, L. H. Wang, S. W. Cheong, I. Radu, C. Ropers, and R. I. Tobey, *J. Phys.: Condens. Matter*, **28**, 356002 (2016).
- ¹⁵ Q. Liu, X. D. Zhu, L. H. Wang, S. W. Cheong, and R. I. Tobey, *J. Phys.: Condens. Matter*, **28**, 194002 (2016).
- ¹⁶ W. J. Hardy, C. -W. Chen, A. Marcinkova, H. Ji, J. Sinova, D. Natelson, and E. Morosan, *Phys. Rev. B* **91**, 054426 (2015).
- ¹⁷ F. T. Huang, and S. W. Cheong, *Nat. Rev. Mater.* **2**, 17004 (2017).
- ¹⁸ M. -H. Whangbo, E. Canadell, P. Foury, and J. P. Pouget, *Science* **252**, 96 (1991).
- ¹⁹ C. C. Homes, A. Akrap, J. S. Wen, Z. J. Xu, Z. W. Lin, Q. Li, and G. D. Gu, *Phys. Rev. B* **81**, 180508(R) (2010).
- ²⁰ Q. M. Si, R. Yu, and E. Abrahams, *Nat. Rev. Mater.* **1**, 1 (2016).
- ²¹ D. S. Inosov, *C. R. Physique* **17**, 60 (2016).
- ²² A. Filippetti, V. Fiorentini, F. Ricci, P. Delugas, and J. Iniguez, *Nat. Comm.* **7**, 11211 (2016).
- ²³ Y. G. Shi, Y. F. Guo, X. Wang, A. J. Princep, D. Khalyavin, P. Manuel, Y. Michiue, A. Sato, K. Tsuda, S. Yu, M. Arai, Y. Shirako, M. Akaogi, N. Wang, K. Yamamura, and A. T. Boothroyd, *Nat. Mater.* **12**, 1024 (2013).
- ²⁴ Atomistix ToolKit version 13.8, QuantumWise A/S (www.quantumwise.com)
- ²⁵ J. M. Soler, E. Artacho, J. D. Gale, A. Garcia, J. Junquera, P. Ordejon, and D. Sanchez-Portal, *J. Phys.: Condens. Matter* **14**, 2745 (2002).
- ²⁶ Energy minimization tolerance of $<10^{-5}$ Hartree with a k -point sampling of $10 \times 10 \times 10$ were used along with potentials of $U_{Ta} = 2.5$ eV and $U_{Fe} = 4.0$ eV.
- ²⁷ A. Meetsma, G. A. Wieggers, R. J. Haange, and J. L. de Boer, *Acta Cryst. C* **46**, 1598 (1990).
- ²⁸ S. S. P. Parkin and R. H. Friend, *Physica* **99b**, 219 (1980).
- ²⁹ J. G. Checkelsky, M. Lee, E. Morosan, R. J. Cava, and N. P. Ong, *Phys. Rev. B* **77**, 014433 (2008).
- ³⁰ M. Naito and S. Tanaka, *J. Phys. Soc. Jpn.* **51**, 219 (1982).
- ³¹ A phonon is also present in the vicinity.
- ³² S. S. P. Parkin and S. C. Bayliss, *J. Phys. C: Solid State Phys.* **15**, 6851 (1982).
- ³³ J. Dijkstra, P. J. Zijlema, C. F. van Bruggen, C. Haas, and R. A. de Groot, *J. Phys.: Condens. Matter* **1**, 6363 (1989).
- ³⁴ L. F. Mattheiss, *Phys. Rev. B* **8**, 3719 (1973).
- ³⁵ R. M. Geilhufe, A. Bouhon, S. S. Borysov, and A. V. Balatsky, *Phys. Rev. B* **95**, 041103 (2017).
- ³⁶ J. R. Schaibley, H. Yu, G. Clark, P. Rivera, J. S. Ross, K. L. Seyler, W. Yao, and X. Xu, *Nature Rev. Mater.* **1**, 16055 (2016).
- ³⁷ W. G. McMullan and J. C. Irwin, *Can. J. Phys.* **62**, 789 (1984).

- ³⁸ These trends are also apparent in the raw reflectance spectra (inset, Fig. 2(c)).
- ³⁹ J. Choi, J. L. Musfeldt, J. He, R. Jin, J. R. Thompson, D. Mandrus, X. N. Lin, V. A. Bondarenko, and J. W. Brill, Phys. Rev. B **69**, 085120 (2004).
- ⁴⁰ B. Monseratt and D. H. Vanderbilt, arXiv:1706.07809 [cond-mat.mtrl-sci] (2017).
- ⁴¹ C. Martin, E. D. Mun, H. Berger, V. S. Zapf, and D. B. Tanner, Phys. Rev. B **87**, 041104 (2013).